Synergistic effects of treating the spinal cord and brain in CLN1 disease

Charles Shyng[a,1], Hemanth R. Nelvagal[b,c,1], Joshua T. Dearborn[a], Jaana Tyynelä[d], Robert E. Schmidt[e], Mark S. Sands[a,f,2], and Jonathan D. Cooper[b,c,g,2]

[a]Division of Oncology, Department of Medicine, Washington University School of Medicine, St. Louis, MO 63110; [b]Department of Basic and Clinical Neuroscience, Maurice Wohl Clinical Neuroscience Institute, Institute of Psychiatry, Psychology & Neuroscience, King's College London, London SE5 9RX, United Kingdom; [c]Department of Pediatrics, Los Angeles Biomedical Research Institute, Harbor-UCLA Medical Center, University of California, Los Angeles, Torrance, CA 90502; [d]Institute of Biomedicine/Biochemistry, University of Helsinki, 00014 Helsinki, Finland; [e]Division of Neuropathology, Department of Pathology & Immunology, Washington University School of Medicine, St. Louis, MO 63110; [f]Department of Genetics, Washington University School of Medicine, St. Louis, MO 63110; and [g]Department of Pediatrics, David Geffen School of Medicine, University of California, Los Angeles, CA 90095

Edited by William S. Sly, Saint Louis University School of Medicine, St. Louis, MO, and approved June 7, 2017 (received for review February 3, 2017)

Infantile neuronal ceroid lipofuscinosis (INCL, or CLN1 disease) is an inherited neurodegenerative storage disorder caused by a deficiency of the lysosomal enzyme palmitoyl protein thioesterase 1 (PPT1). It was widely believed that the pathology associated with INCL was limited to the brain, but we have now found unexpectedly profound pathology in the human INCL spinal cord. Similar pathological changes also occur at every level of the spinal cord of PPT1-deficient (*Ppt1*$^{-/-}$) mice before the onset of neuropathology in the brain. Various forebrain-directed gene therapy approaches have only had limited success in *Ppt1*$^{-/-}$ mice. Targeting the spinal cord via intrathecal administration of an adeno-associated virus (AAV) gene transfer vector significantly prevented pathology and produced significant improvements in life span and motor function in *Ppt1*$^{-/-}$ mice. Surprisingly, forebrain-directed gene therapy resulted in essentially no PPT1 activity in the spinal cord, and vice versa. This leads to a reciprocal pattern of histological correction in the respective tissues when comparing intracranial with intrathecal injections. However, the characteristic pathological features of INCL were almost completely absent in both the brain and spinal cord when intracranial and intrathecal injections of the same AAV vector were combined. Targeting both the brain and spinal cord also produced dramatic and synergistic improvements in motor function with an unprecedented increase in life span. These data show that spinal cord pathology significantly contributes to the clinical progression of INCL and can be effectively targeted therapeutically. This has important implications for the delivery of therapies in INCL, and potentially in other similar disorders.

infantile Batten disease | adeno-associated virus | spinal cord | brain | combination therapy

The neuronal ceroid lipofuscinoses (NCLs) are monogenic, predominantly autosomal-recessive, and progressive neurodegenerative lysosomal storage disorders (LSDs), which mainly present in childhood. Collectively, the NCLs are the most common inherited neurological disease of children (1). Because no effective treatments are currently available, all forms of NCL are fatal (2, 3). Classic CLN1 disease or infantile NCL (INCL) is caused by autosomal-recessive mutations in the *PPT1* gene (4, 5). This encodes palmitoyl protein thioesterase 1 (PPT1), a lysosomal enzyme that catalyzes the cleavage of thioester bonds linking long-chain fatty acids to proteins (6, 7). CLN1 disease is a very severe and rapidly progressing form of NCL, presenting as early as 6 to 24 mo of age. Affected children display a rapid loss of motor function, visual acuity, and cognitive abilities and a greatly reduced life expectancy of between 9 and 13 y (8, 9).

PPT1-deficient mice (*Ppt1*$^{-/-}$) exhibit a CLN1 disease-like phenotype including retinal dysfunction, progressive sensorimotor defects, seizures, and a shortened life span (10–12). These mice have been a powerful tool to study functional deficits, as well as pathology, in the forebrain and cerebellum. The brains of *Ppt1*$^{-/-}$ mice showed reduced brain volume (13), progressive cerebral atrophy, and regional neuron loss, all preceded by glial activation (11, 14). Neurons also showed the characteristic accumulation of autofluorescent storage material (AFSM) within their cell bodies (11). Similar reactive and degenerative changes occur in the cerebellum (15), and there is evidence for both axonal and synaptic pathology (16). However, these findings cannot fully explain the sensorimotor deficits observed both in patients and *Ppt1*$^{-/-}$ mice (17, 18).

Various experimental therapies have been tested to treat forebrain pathology in *Ppt1*$^{-/-}$ mice, including antioxidants (19, 20), enzyme replacement therapy (ERT) (21, 22), human neuronal stem cells (23), and forebrain-directed gene therapy (12, 24–27). Of these, adeno-associated virus (AAV) vector-mediated gene transfer has been the most promising (3, 28). However, these therapies have met with only limited success, especially compared with efforts in CLN2 disease, another form of NCL caused by a lysosomal enzyme deficiency (29, 30).

To investigate an anatomical basis for the sensorimotor deficits seen in *Ppt1*$^{-/-}$ mice and to explain the relatively poor efficacy of forebrain-targeted therapies, we postulated the existence of neuropathology outside the brain. We focused our analysis on the spinal cord as a key component of the sensory and motor pathways. Although the spinal cord has not previously been characterized in detail in any form of NCL, our recent analysis of intrathecally delivered enzyme replacement therapy had revealed significant end-stage pathology in the spinal cords of *Ppt1*$^{-/-}$ mice (31). This prompted us to investigate the onset and progression of this spinal

Significance

Infantile neuronal ceroid lipofuscinosis (INCL, or infantile Batten disease) is a fatal childhood disease that devastates the brain. Trying to treat the brain alone has so far proved ineffective, so we looked for effects of the disease in other parts of the body. Unexpectedly, we found that the spinal cord is severely affected before the brain and contributes to disease outcome. Directing gene therapy to just the spinal cord of INCL mice can improve their disease. However, treating both the spinal cord and brain provides the most effective therapeutic strategy ever seen in this disease. This combined therapy returned INCL mice to a near-normal life span and dramatically improved their quality of life.

Author contributions: C.S., H.R.N., M.S.S., and J.D.C. designed research; C.S., H.R.N., and J.T.D. performed research; J.T. and R.E.S. contributed new reagents/analytic tools; C.S. and H.R.N. analyzed data; and C.S., H.R.N., M.S.S., and J.D.C. wrote the paper.

The authors declare no conflict of interest.

This article is a PNAS Direct Submission.

Freely available online through the PNAS open access option.

[1]C.S. and H.R.N. contributed equally to this work.

[2]To whom correspondence may be addressed. Email: msands@dom.wustl.edu or jonathan.cooper@labiomed.org.

This article contains supporting information online at www.pnas.org/lookup/suppl/doi:10.1073/pnas.1701832114/-/DCSupplemental.

pathology and how it relates to the well-defined sequence of events in the forebrain of these mice. This novel temporal analysis revealed unexpectedly early and profound neuropathological changes that occur at all levels of the cord of *Ppt1*$^{-/-}$ mice. These changes started at an age when there were few neurodegenerative changes seen in the brains of these mice. Crucially, similar pathology was also present in human CLN1 spinal cord autopsy material.

This novel finding of early and profound pathology throughout the spinal cord led us to investigate whether it was possible to target this region therapeutically by means of AAV-mediated gene therapy using a third-generation AAV2/9 vector (32, 33). Therefore, we tested whether intrathecal (IT) injections of an AAV2/9-hPPT1 vector, either alone or in combination with intracranial (IC) injections (12, 24–27), would have any beneficial effect on disease progression and brain and spinal cord pathology.

Results

Human CLN1 Spinal Cord Displays Profound Neuropathological Changes. To investigate whether similar pathological changes occur in the spinal cord of human CLN1 disease as those found in the brain

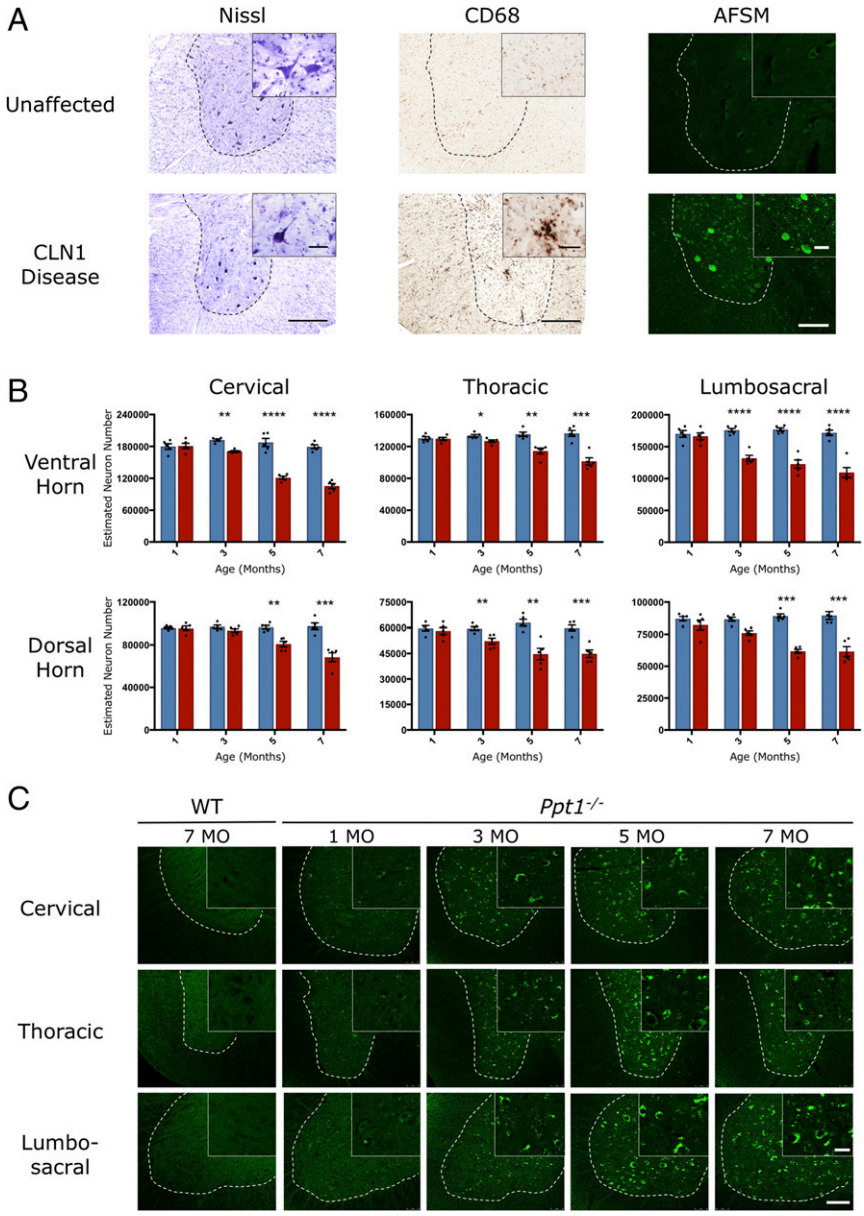

Fig. 1. Spinal cord pathology in human and murine CLN1 disease. (*A*) Representative bright-field images of ventral horns (demarcated by the dotted lines) of human thoracic spinal cord showing fewer, more darkly stained neurons (Nissl), an increase in the number of hypertrophied microglia (CD68), and representative confocal microscopy images showing pronounced accumulation of autofluorescent storage material in human post mortem CLN1 disease tissue compared with an unaffected control. [Scale bars, 200 μm (bright field, *Left and Center*), 100 μm (confocal, *Right*), and 25 μm (*Insets*).] (*Insets*) Selected from corresponding lower-power views. (*B*) Unbiased optical fractionator counts reveal significant loss of Nissl (cresyl fast violet)-stained neurons in the dorsal and ventral horns of the spinal cords of PPT1-deficient (red bars) mice as early as 3 mo of age, compared with age-matched wild-type controls (blue bars). Dots represent scatterplots of individual animals. *$P < 0.05$, **$P < 0.01$, ***$P < 0.001$, ****$P < 0.0001$, two-tailed, unpaired parametric *t* test. Values are shown as mean ± SEM ($n = 5$ mice per group). (*C*) Representative confocal microscopy images of unstained sections showing the progressive accumulation of autofluorescent storage material (green) within morphologically identified neuronal cell bodies in the ventral horns (represented by the dotted lines) of the lumbosacral cord of *Ppt1*$^{-/-}$ mice as early as 3 mo, compared with age-matched wild-type controls. [Scale bars, 100 μm and 25 μm (*Insets*).] (*Insets*) Selected from corresponding lower-power views.

(34), we obtained spinal cord sections from a single 6-y-old diseased case and a 10-y-old neurologically normal spinal cord. Nissl staining revealed fewer neurons present in human CLN1 tissue, and those that persisted displayed a range of abnormal morphologies, being either distended by accumulated storage material or darkened and shrunken (Fig. 1*A*). CD68 staining for microglia revealed the presence of many darkly stained and hypertrophied microglia in the CLN1 disease case (Fig. 1*A*). These activated microglia were predominantly within the gray matter, but were also present in white matter tracts. As expected, the few remaining neurons displayed massive amounts of autofluorescent storage material (Fig. 1*A*). In addition, many smaller cells, morphologically identified as microglia, also displayed pronounced levels of storage material. These changes reveal that pronounced neuropathological changes occur in the spinal cord in this disorder. This unexpected finding led us to systematically investigate the temporal and spatial progression of spinal pathology in *Ppt1*$^{-/-}$ mice.

Early and Widespread Neuron Loss in *Ppt1*$^{-/-}$ Mouse Spinal Cords. Pronounced neuron loss is an important feature of CLN1 disease, and becomes significant within the cerebellum and thalamus of *Ppt1*$^{-/-}$ mice by 5 mo (14, 15). We obtained unbiased optical fractionator counts of Nissl-stained neurons in the dorsal and ventral horns, at all levels of the spinal cord of control and *Ppt1*$^{-/-}$ mice at different ages. These data revealed a significant loss of neurons at all three levels (cervical, lumbosacral dorsal horn, and thoracic ventral horn) of the cord, sometimes as early as 3 mo (Fig. 1*B*). Regardless of rostrocaudal level, there was invariably a significant loss of neurons both in the dorsal and ventral horns in *Ppt1*$^{-/-}$ mice from 5 mo of age onward. There was also significant neuron loss at 3 mo of age in both the dorsal and ventral horns, indicating an earlier onset of neurodegenerative changes in the spinal cord compared with the brain (14).

Progressive Accumulation of Autofluorescent Storage Material in *Ppt1*$^{-/-}$ Mouse Spinal Cords. Progressive accumulation of AFSM within cell bodies is pathognomic of the NCLs (1, 9). This provides a useful diagnostic readout of the extent of pathology. In *Ppt1*$^{-/-}$ mice, the characteristic punctate appearance of this autofluorescent storage material was already evident at 3 mo in the cell bodies within spinal gray matter of the dorsal and ventral horns, and occurred to a similar extent at all levels (Fig. 1*C*).

***Ppt1*$^{-/-}$ Mouse Spinal Cords Show Progressive Glial Activation at All Levels.** Astrocytosis and microglial activation are closely associated with neuron loss in the forebrains of *Ppt1*$^{-/-}$ mice, typically preceding neurodegeneration (14). Immunostaining sections of cervical, thoracic, and lumbar cord for CD68 (typically used as a marker of microglial activation by revealing the associated changes in microglial morphology and increased staining intensity) and glial fibrillary associated protein (GFAP; typically used as a marker of astrocytosis by revealing the associated changes in astrocyte morphology and increased staining intensity) (Fig. 2) revealed a profound and early-onset glial activation at all levels of the *Ppt1*$^{-/-}$ spinal cord. From 3 mo onward, *Ppt1*$^{-/-}$ mice displayed a dramatic increase in the intensity of CD68 staining (Fig. 2*A*), with many more of these cells displaying the typical hypertrophied morphology of brain macrophages. Although most pronounced throughout the gray matter, increasingly more intensely stained and hypertrophied microglia were also present in the *Ppt1*$^{-/-}$ spinal white matter from 5 mo onward. This white matter microgliosis appeared more pronounced in the dorsal compared with the ventral funiculi, but was present at all rostrocaudal levels of the *Ppt1*$^{-/-}$ spinal cord (Fig. 2*A*). Both wild-type and *Ppt1*$^{-/-}$ mice exhibited intense GFAP staining of fibrous astrocytes within all white matter tracts at all ages examined. From 3 mo of age onward in the *Ppt1*$^{-/-}$ mouse spinal cord, numerous intensely GFAP-stained astrocytes with hypertrophied cell bodies and relatively few thickened processes

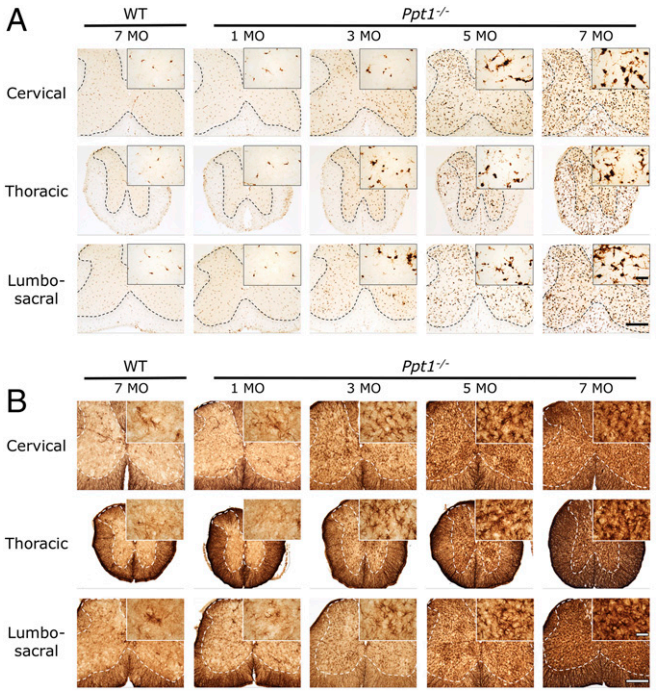

Fig. 2. *Ppt1*$^{-/-}$ mouse spinal cord shows progressive glial activation at all levels. Representative bright-field microscopy images of the spinal cords of *Ppt1*$^{-/-}$ and wild-type control mice reveal the increased abundance, hypertrophy, and increased staining intensity of CD68-positive microglia (*A*) and GFAP-positive astrocytes (*B*) in mutant mice as early as 3 mo of age at all levels of the spinal cord. This glial activation progressively increases with age. The dotted lines demarcate the boundary between the gray and white matter. [Scale bars, 200 μm and 25 μm (*Insets*).] (*Insets*) Selected from corresponding lower-power views.

were present throughout the spinal gray matter, with no obvious laminar specificity. From 5 mo onward, the entire spinal gray matter of *Ppt1*$^{-/-}$ mice was completely filled with highly activated astrocytes (Fig. 2*B*).

Intracranial and Intrathecal Injections of AAV2/9-hPPT1 Deliver PPT1 Activity to the Brain and Spinal Cord, Respectively. To determine whether this spinal cord disease could be effectively targeted therapeutically, *Ppt1*$^{-/-}$ mice were injected intrathecally with an AAV vector (IT-AAV2/9-hPPT1) to target the cord, intracranially (IC-AAV2/9-hPPT1) to target the brain, or a combination of the two delivery routes (IC/IT-AAV2/9-hPPT1). At 1 mo of age, supraphysiological levels of PPT1 activity were detected in the spinal cords of mice receiving IT-AAV2/9-hPPT1 alone (Fig. 3*A*), whereas the brains of these intrathecally treated mice had only ∼10% of normal levels. A reciprocal pattern of enzyme activity was seen in PPT1-deficient mice injected solely with IC-AAV2/9-hPPT1, where these mice had supraphysiological or WT levels of PPT1 activity in their brains but nearly undetectable levels of PPT1 activity in their spinal cords (Fig. 3*A*).

To determine whether this viral-mediated expression was persistent, PPT1 activity was measured in 7-mo-old mouse brains (Fig. 3*B*). PPT1 activity was virtually undetectable in the brains of untreated *Ppt1*$^{-/-}$ mice compared with wild-type mice. There was ∼2 to 5% of wild-type PPT1 activity in the brains of mice receiving IT-AAV2/9-hPPT1 (Fig. 3*B*). There was no significant difference between IC-AAV2/9-hPPT1–only and IC/IT-AAV2/9-hPPT1 combination-treated PPT1 brain activities compared with WT at all of the time points examined (3, 5, 7, and 9 mo; Fig. 3*B* and Fig. S1*A*). Similar results were observed when mice from these treatment groups were stained using a recently developed

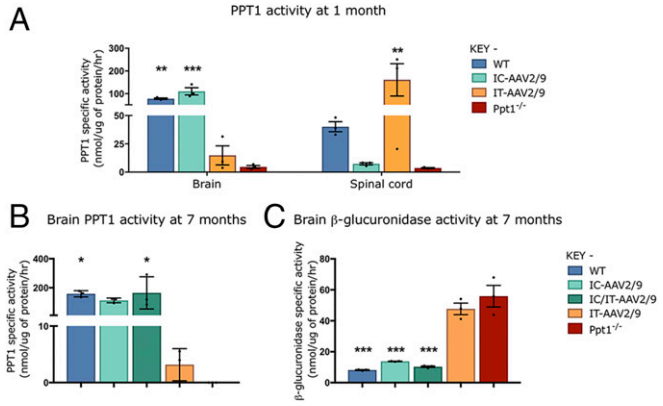

Fig. 3. Changes in PPT1 and secondary enzyme activity in regions targeted with AAV2/9-mediated gene therapy. There were reciprocal increases in PPT1 activity between intrathecally (IT-AAV2/9) and intracranially (IC-AAV2/9) injected mice in the spinal cord and brain, respectively, at 1 mo (*A*). PPT1 levels in the brains of wild-type and IC-AAV2/9–injected mice were significantly increased compared with $Ppt1^{-/-}$, whereas IT-AAV2/9–injected mice showed significantly elevated levels of PPT1 in the spinal cord. At 7 mo, the brains of IC-AAV2/9 and combination-treated mice (IC/IT-AAV2/9) show significant increases in PPT1 activity (*B*) and significant decreases in β-glucuronidase activity (*C*), similar to WT mice, compared with $Ppt1^{-/-}$ mice. Dots represent scatterplots of individual animals. $^{*}P < 0.05$, $^{**}P < 0.01$, $^{***}P < 0.001$, one-way ANOVA with post hoc Bonferroni correction. Values shown are mean ± SEM ($n = 3$ mice per group).

histochemical stain for PPT1 (35) [Figs. S2 (forebrain) and S3 (spinal cord)].

A reduction in the secondary elevation of other lysosomal enzymes serves as a biochemical surrogate of therapeutic efficacy in PPT1-deficient mice (24). At 7 mo of age, there was a significant increase in brain β-glucuronidase (GUSB) activity in untreated $Ppt1^{-/-}$ mice (Fig. 3*C*). This secondary elevation of GUSB activity persisted in the brains of PPT1-deficient mice receiving IT-AAV2/9 alone. However, there was a significant decrease in brain GUSB activity in mice receiving either IC-AAV2/9-hPPT1 alone or IC/IT-AAV2/9-hPPT1 combined treatment (Fig. 3*C*). Brain GUSB activity was not significantly different between WT, IC-AAV2/9-hPPT1–only, and IC/IT-AAV2/9-hPPT1 combination-treated mice at 7 mo. As with PPT1 activity, these patterns of GUSB activity were consistent across every time point examined (3, 5, 7, and 9 mo; Fig. S1*B*).

Combination IC/IT-AAV2/9-hPPT1 Gene Therapy Synergistically Improves Life Span and Prolongs Motor Function in $Ppt1^{-/-}$ Mice. All treatment groups showed a significant increase in median life span compared with untreated $Ppt1^{-/-}$ mice (~8.4 mo). Combination IC/IT-AAV2/9-hPPT1–treated mice had the longest median life span of 19.3 mo, with the longest-lived mouse at 22 mo, compared with IC-AAV2/9-hPPT1–injected mice (median 13.6 mo) or IT-AAV2/9-hPPT1–injected mice (median 11.8 mo) (Fig. 4*A*). Rotarod testing revealed that IC/IT-AAV2/9-hPPT1 mice performed better for much longer than either IC-AAV2/9-hPPT1 or IT-AAV2/9-hPPT1 mice (Fig. 4*B*). However, all treated animals performed better than their untreated counterparts from 7 mo on (Fig. 4*B*). At 5 mo of age, when there is significant pathology in both the brain and spinal cord, there was no evidence of a learning deficit during the training/acclimation phase of the rotarod test in any group.

AAV2/9-Mediated Gene Therapy Rescues Cortical Atrophy and Delays Neuron Loss in $Ppt1^{-/-}$ Mice. Profound brain atrophy is a hallmark of CLN1 disease (11, 13, 14), and cortical thickness (Fig. 4*C*) and brain weight (Fig. 4*D*) were measured as indicators of this process. There was a significant thinning of the cerebral cortex in untreated $Ppt1^{-/-}$ and IT-AAV2/9-hPPT1–treated mice compared with wild-type controls. However, cortical thinning was effectively halted in IC-AAV2/9-hPPT1– and IC/IT-AAV2/9-hPPT1–treated mutant mice (Fig. 4*C*). The weight of the $Ppt1^{-/-}$ mouse brain gradually decreases with disease progression (11, 14). The decrease in brain weight of mice treated with IT-AAV2/9-hPPT1 was similar to that seen in untreated $Ppt1^{-/-}$ mice in both magnitude and rate (Fig. 4*D*). Brain weight was maintained at nearly normal levels in both the IC-AAV2/9-hPPT1 alone and IC/IT-AAV2/9-hPPT1 combination treatment groups for up to 9 mo (Fig. 4*D*).

Severe and progressive neuron loss is another hallmark of CLN1 disease (14, 15). Consistent with these previous observations, there was a significant and progressive loss of neurons in the primary motor cortex (M1), ventral posterior thalamic nuclei (VPM/VPL), and ventral horn of the lumbosacral spinal cord (LSC) of untreated $Ppt1^{-/-}$ mice (Fig. 4*E*). All treatment groups showed significant improvements in M1 cortical neuron counts at 3 and 7 mo (Fig. 4*E*). The VPM/VPL are more severely affected in $Ppt1^{-/-}$ mice (11, 14), and neuron loss in this region was broadly comparable in all treatment groups to that observed in untreated $Ppt1^{-/-}$ mice regardless of age (Fig. 4*E*). However, the neuron loss in the LSC at 7 mo of age was significantly less in the IT-AAV2/9-hPPT1–only and IC/IT-AAV2/9-hPPT1 combination treatment groups compared with untreated $Ppt1^{-/-}$ mice. At 9 mo of age, when all untreated $Ppt1^{-/-}$ mice had already died, there was no significant difference in LSC neuron counts between WT controls and the IC/IT-AAV2/9-hPPT1–treated $Ppt1^{-/-}$ mice (Fig. S4*A*). These data show that AAV-mediated gene therapy had a significant neuroprotective effect in the regions where it was targeted in $Ppt1^{-/-}$ mice.

IC and IT Delivery of Gene Therapy Differentially Reduce AFSM in the Brains and Spinal Cords of $Ppt1^{-/-}$ Mice. As expected, there was an increase in AFSM at every age examined in all regions of untreated $Ppt1^{-/-}$ brains compared with WT controls (Fig. 5*A*). In the M1 cortex, both IC-AAV2/9-hPPT1– and IC/IT-AAV2/9-hPPT1–treated mice showed reduced AFSM levels, but these did not reach statistical significance, compared with IT-AAV2/9-hPPT1 mice (Fig. 5*B*). Although all treatment groups showed levels of AFSM accumulation that were higher than wild-type controls, this was much lower than in untreated $Ppt1^{-/-}$ mice. In the VPM/VPL, all of the treatment groups had an apparent decrease in AFSM at 3 and 5 mo compared with untreated $Ppt1^{-/-}$ mice (Fig. 5*A*). At 5 and 7 mo, IC-AAV2/9-hPPT1– and IC/IT-AAV2/9-hPPT1–treated mice appeared to have the greatest decrease in AFSM in the VPM/VPL (Fig. 5*A*), but this was not statistically significant (Fig. 5*B*). In the lumbar spinal cord, both IC/IT-AAV2/9-hPPT1 and IT-AAV2/9-hPPT1 mice showed AFSM levels comparable to wild-type controls, whereas IC-AAV2/9-hPPT1 mice showed similar amounts of AFSM accumulation to untreated $Ppt1^{-/-}$ mice (Fig. 5). At 9 mo, only IT-AAV2/9-hPPT1 and IC-AAV2/9-hPPT1 mice showed a significantly higher level of AFSM compared with the wild type in the M1 cortex and lumbar spinal cord, respectively (Fig. S4*B*).

Combination IC/IT-AAV2/9 Gene Therapy Reduces Neuroinflammation in $Ppt1^{-/-}$ Mice. Progressive microglial activation and astrocytosis are prominent features of CLN1 disease, and can be quantified by thresholding image analysis (11, 14). As before (Fig. 2), untreated $Ppt1^{-/-}$ mice showed a significant increase in CD68 and GFAP staining in the brain and lumbosacral spinal cord compared with wild-type mice at every time point (Figs. 6*A* and 7*A*). This was confirmed by thresholding image analysis (Figs. 6*B* and 7*B*). In the brains of mice treated with IC-AAV2/9-hPPT1 alone or the IC/IT-AAV2/9-hPPT1 combination, there was an apparent decrease in CD68 and GFAP staining in the M1 cortex at every time point (Figs. 6 and 7 and Fig. S5). There was also a moderate decrease in CD68 staining in the M1 cortex of mice receiving IT-AAV2/9-hPPT1 alone at 3 and 5 mo of age, but this decrease was not sustained at 7 mo (Fig. 6*B*). There was a significant impact upon

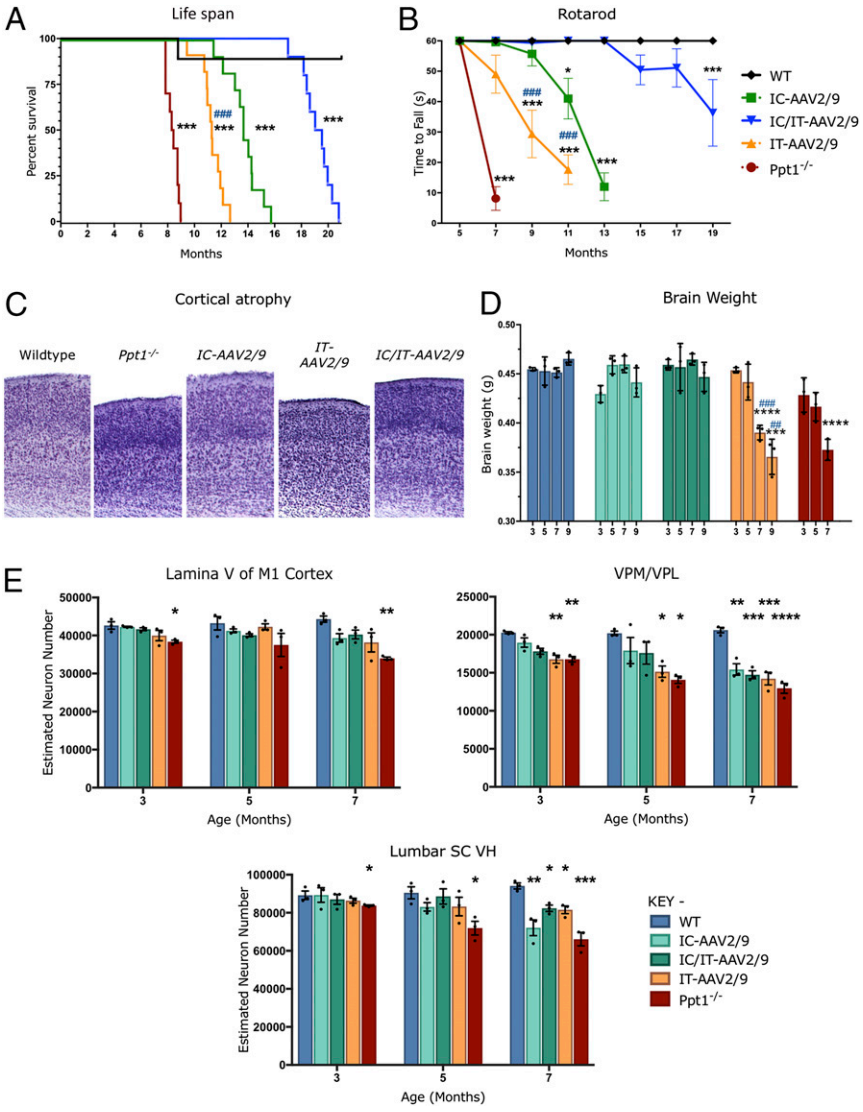

Fig. 4. Targeted AAV2/9-mediated gene therapy delays disease progression and prevents neuron loss. (*A*) Kaplan–Meier survival curve showing that the median life span for combination IC/IT-treated mice (IC/IT-AAV2/9) (blue) is significantly greater than either intrathecally (IT-AAV2/9) (yellow) or intracranially (IC-AAV2/9) treated mice (green) ($n = 10$ mice per group). Analysis by log-rank test for trend was significant for overall survival ($P < 0.0001$). Individual comparisons between curves, using Bonferroni correction for multiple comparisons, were each significant (***$P < 0.001$) for each group compared with the wild type, as well as between intrathecally (IT-AAV2/9) and intracranially (IC-AAV2/9) treated mice ($^{###}P < 0.001$). (*B*) Constant-speed rotarod test revealed that untreated *Ppt1*$^{-/-}$ mice (red) were unable to stay on the rotarod past 7 mo, intrathecally (IT-AAV2/9) treated mice (yellow) could not stay on the rotarod past 11 mo, intracranially (IC-AAV2/9) treated mice (green) could not stay on the rotarod past 13 mo, and combination IC/IT-treated mice (IC/IT-AAV2/9) (blue) showed deficits at 15 mo and could not stay on the rotarod past 19 mo. Statistical significance for each group compared with wild-type mice (*$P < 0.05$, ***$P < 0.001$), and compared between intrathecally (IT-AAV2/9) and intracranially (IC-AAV2/9) treated mice ($^{###}P < 0.001$), two-way repeated-measure ANOVA ($n = 10$ mice per group). (*C*) Representative images of cortices from treated animals in Nissl (cresyl fast violet)-stained sections showing near–wild-type thickness of IC-AAV-2/9– and IC/IT-AAV2/9–treated mouse cortices but not in IT-AAV2/9–treated mice. (*D*) Brain weights for IC-AAV2/9– and IC/IT-AAV2/9–treated mice were essentially the same as WT mice at all time points examined. However, IT-AAV2/9–treated and untreated *Ppt1*$^{-/-}$ mice showed a significant reduction in brain weight compared with WT brain weight at 7 and 9 mo. Dots represent scatterplots of individual animals. Significance is compared with wild-type mice (***$P < 0.001$, ****$P < 0.0001$), and compared between intrathecally (IT-AAV2/9) and intracranially (IC-AAV2/9) treated mice ($^{##}P < 0.01$, $^{###}P < 0.001$), two-way repeated-measure ANOVA ($n = 3$ mice per group). (*E*) Unbiased optical fractionator counts of Nissl (cresyl fast violet)-stained neurons at 3, 5, and 7 mo post injection in the M1 motor cortex, VPM/VPL of the thalamus, and ventral horn (VH) of the lumbar spinal cord show that targeted AAV-2/9–mediated gene therapy has a neuroprotective effect. Significance is compared with untreated WT mice at all time points. Dots represent scatterplots of individual animals. *$P < 0.05$, **$P < 0.01$, ***$P < 0.001$, ****$P < 0.0001$, one-way ANOVA with post hoc Bonferroni correction. Values shown are mean ± SEM ($n = 3$ mice per group).

CD68 staining in the thalamus of IC-AAV2/9-hPPT1–treated mice at 5 and 7 mo and for IC/IT-AAV2/9-hPPT1 mice at 5 mo (Fig. 6). In contrast, there was no significantly lower GFAP staining across any of the treatment groups in the thalamus regardless of age (Fig. 7). In the lumbosacral cord of mutant mice treated with IT-AAV2/9-hPPT1 or IC/IT-AAV2/9-hPPT1 at 3, 5, and 7 mo, there appeared to be a dramatic decrease in both CD68 and GFAP staining (Figs. 6 and 7), with accompanying effects on the morphological appearance of these microglia (Fig. 6*A*). Mutant mice treated with IC-AAV2/9-hPPT1 alone also had decreased CD68 staining in the lumbosacral spinal cord at 3 mo of age but not at 5 or 7 mo (Fig. 6*B*). There was no decrease in GFAP staining in the lumbosacral spinal cord at any age following IC-AAV2/9-hPPT1 only (Fig. 7). At 9 mo, IC-AAV2/9-hPPT1–treated mice showed a significant increase in CD68 staining in the thalamus and LSC, as well as a significant increase of GFAP staining in

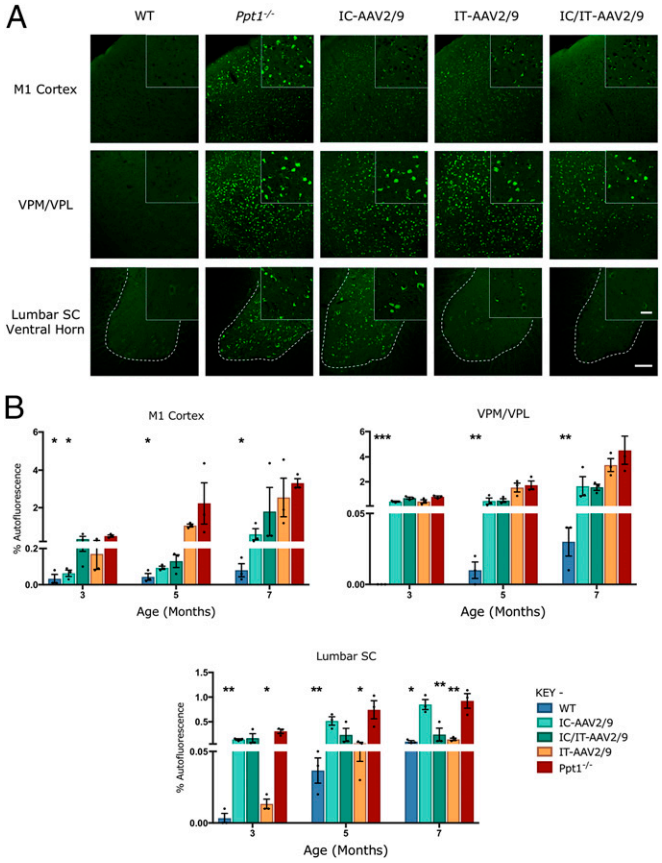

Fig. 5. Targeted gene therapy reduces storage material accumulation in *Ppt1*$^{-/-}$ mice. (*A*) Representative confocal microscopy images of treated animals and controls at 7 mo showing the primary motor cortex, VPM/VPL of the thalamus, and ventral horn of the lumbar spinal cord with differential patterns of reduction of autofluorescent storage material accumulation in intracranially (IC-AAV2/9), intrathecally (IT-AAV2/9), and combination intracranially and intrathecally (IC/IT-AAV2/9) treated mice, compared with untreated *Ppt1*$^{-/-}$ and wild-type control mice. IC/IT-AAV2/9 mice show an overall greater reduction in AFSM than either IC-AAV2/9 or IT-AAV2/9 therapy alone. The dotted lines demarcate the boundary between the gray and white matter in spinal cord sections. [Scale bars, 100 μm and 25 μm (*Insets*).] (*Insets*) Selected from corresponding lower-power views. (*B*) Thresholding image analysis at 3-, 5-, and 7-mo time points showing a significant but differential pattern of the reduction of AFSM accumulation based on the site of vector administration, with IC/IT-treated mice showing the greatest overall reduction of AFSM. Significance is compared with untreated *Ppt1*$^{-/-}$ mice. Dots represent scatterplots of individual animals. $*P < 0.05$, $**P < 0.01$, $***P < 0.001$, one-way ANOVA with post hoc Bonferroni correction. Values shown are mean ± SEM ($n = 3$ mice per group).

the thalamus (Fig. S5). Reciprocally, IT-AAV2/9-hPPT1–treated mice showed significantly higher levels of CD68 and GFAP staining in the M1 cortex and VPM/VPL. However, IC/IT-AAV2/9-hPPT1–treated mice did not show any significant change from WT mouse levels of CD68 or GFAP staining, with the exception of GFAP staining in the VPM/VPL (Fig. S5).

Cytokine and chemokine levels in whole-brain homogenates of treated mice and controls were measured as a complementary indicator of neuroinflammation (36, 37). At 7 mo of age, there were no significant differences in the levels of tumor necrosis factor α (TNF-α) or IFN-γ between any of the control or treatment groups (Fig. 8*A*). For both the CXC-motif and CCL-motif chemokines, there was a significant increase in untreated *Ppt1*$^{-/-}$ brains compared with wild-type brains. Neither IC-AAV2/9-hPPT1– nor IT-AAV2/9-hPPT1–treated mice showed reduced chemokine levels below that of untreated *Ppt1*$^{-/-}$ brains. There was an apparent increase above *Ppt1*$^{-/-}$ chemokine levels for IT-AAV2/9-hPPT1 mice in CXCL1, CXCL10, CCL2, and CCL7. However, in the brains of IC/IT-AAV2/9-hPPT1 combination-treated *Ppt1*$^{-/-}$ mice, there was a dramatic and significant decrease in nearly all of the chemokines measured to near–wild-type levels (Fig. 8 *B* and *C*).

These data show that AAV2/9-hPPT1 therapy significantly reduces neuroinflammation in the region to which it is targeted, especially in the case of GFAP and CD68 up-regulation. Indeed, combining IC and IT administration of AAV2/9-hPPT1 therapy has a powerful synergistic effect upon multiple measures of disease outcome.

Discussion

The brain has always been considered the main locus of pathology in CLN1 disease (4, 34, 38). However, compared with promising data obtained for another form of NCL, CLN2 disease (32, 33, 39), previous attempts to treat *Ppt1*$^{-/-}$ mice by targeting the known

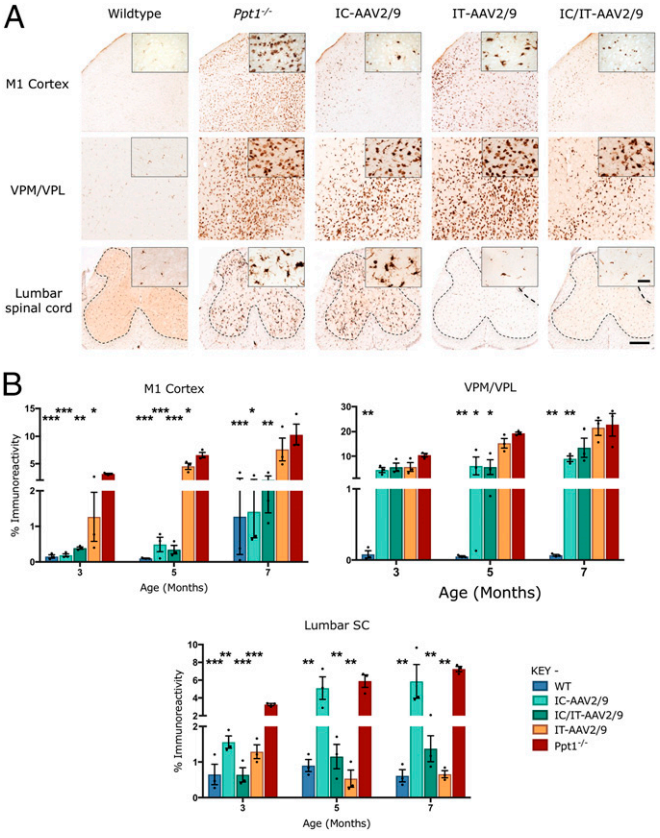

Fig. 6. Targeted gene therapy reduces microglial activation in *Ppt1*$^{-/-}$ mice. (*A*) Representative images of CD68 staining in treated animals and controls at 7 mo. CD68 staining was examined in the primary motor cortex, VPM/VPL of the thalamus, and ventral horn of the lumbar spinal cord showing differential patterns of reduction of microglial activation in intracranially (IC-AAV2/9), intrathecally (IT-AAV2/9), and combination intracranially and intrathecally (IC/IT-AAV2/9) treated mice, compared with untreated *Ppt1*$^{-/-}$ and wild-type control mice. IC/IT-AAV2/9 mice showed an overall greater reduction in microglial activation than either IC-AAV2/9 or IT-AAV2/9 therapy alone. The dotted lines demarcate the boundary between the gray and white matter in spinal cord sections. [Scale bars, 200 μm and 25 μm (*Insets*).] (*Insets*) Selected from corresponding lower-power views. (*B*) Thresholding image analysis at 3-, 5-, and 7-mo time points revealed a significant but region-specific pattern in the impact upon microglial activation based on the site of vector administration, with IC/IT-AAV2/9–treated mice showing the greatest overall reduction of microglial activation. Significance is compared with untreated *Ppt1*$^{-/-}$ mice. Dots represent scatterplots of individual animals. $*P < 0.05$, $**P < 0.01$, $***P < 0.001$, one-way ANOVA with post hoc Bonferroni correction. Values shown are mean ± SEM ($n = 3$ mice per group).

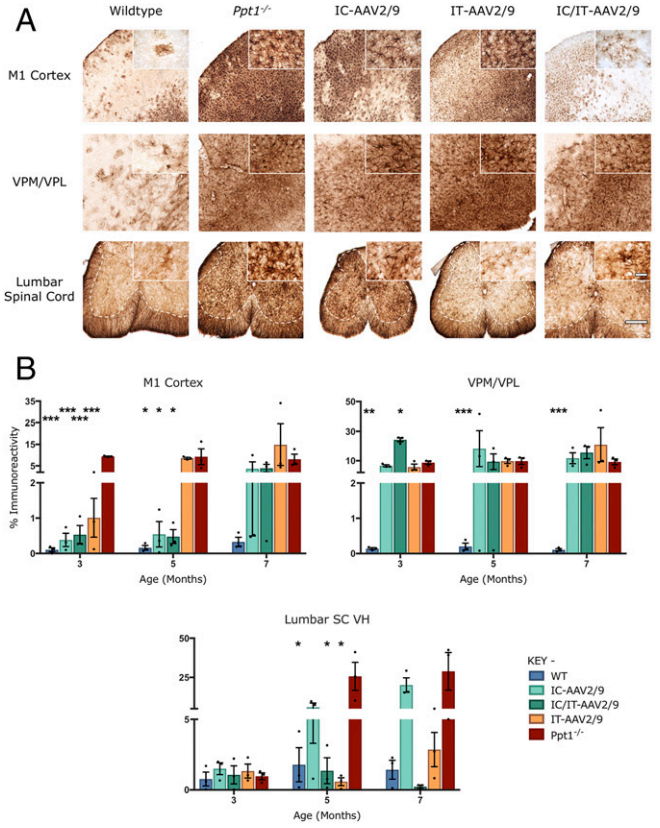

Fig. 7. Combination gene therapy reduces astrocytosis in *Ppt1*$^{-/-}$ mice. (*A*) Representative images of GFAP staining in treated animals and controls at 7 mo, examined in the primary motor cortex, VPM/VPL of the thalamus, and ventral horn of the lumbar spinal cord, showing differential patterns of reduction of astrocytosis in intracranially (IC-AAV2/9), intrathecally (IT-AAV2/9), and combination intracranially and intrathecally (IC/IT-AAV2/9) treated *Ppt1*$^{-/-}$ mice, compared with untreated *Ppt1*$^{-/-}$ and wild-type control mice. IC/IT-AAV2/9 mice showed an overall greater reduction in astrocytosis than either IC-AAV2/9 or IT-AAV2/9 therapy alone. The dotted lines demarcate the boundary between the gray and white matter in spinal cord sections. [Scale bars, 200 μm and 25 μm (*Insets*).] (*Insets*) Selected from corresponding lower-power views. (*B*) Thresholding image analysis at 3-, 5-, and 7-mo time points showing a significant but treatment-specific pattern of the reduced astrocytosis based on the site of vector administration, with IC/IT-AAV2/9–treated mice showing the greatest overall reduction of astrocytosis. Significance is compared with untreated *Ppt1*$^{-/-}$ mice. Dots represent scatterplots of individual animals. **P* < 0.05, ***P* < 0.01, ****P* < 0.001, one-way ANOVA with post hoc Bonferroni correction. Values shown are mean ± SEM (*n* = 3 mice per group).

sites of pathology in the forebrain and cerebellum have had relatively limited success (3, 28). Therefore, we hypothesized the presence of pathology in other regions of the central nervous system that were not affected by these treatments. To better understand the early sensorimotor changes that occur in *Ppt1*$^{-/-}$ mice (18), we focused our analysis on the spinal cord, a structure that has not been seriously considered as a site of pathology in any major form of NCL (38) but in which we had previously seen pathology in end-stage PPT1-deficient mice (31). We have expanded upon the original brief description of the cellular pathology in the human CLN1 spinal cord (4, 34), and revealed that pathology in this region is not only more profound than initially anticipated but also occurs surprisingly early in disease progression in *Ppt1*$^{-/-}$ mice. Indeed, the regional atrophy, loss of different neuron populations, profound glial response, and accumulation of autofluorescent storage material that occur in the brains of these mice (11, 13, 14) all occur to a similar extent in the spinal cord, but at an earlier stage of disease progression. Finding such surprisingly severe and early-onset pathology in a structure that has been relatively neglected analytically suggested to us that the spinal cord may significantly contribute to disease progression and would therefore need to be targeted therapeutically to increase the chances of a positive outcome.

To further improve the efficacy of gene therapy in *Ppt1*$^{-/-}$ mice, we used a third-generation AAV vector (AAV2/9), which is capable of broader distribution within the parenchyma of the brain and increased transduction of neuronal lineages compared with previous generations of AAV vectors (32, 33, 40). Based on a previous study that showed that intrathecal delivery of recombinant PPT1 enzyme could minimally improve the disease phenotype of *Ppt1*$^{-/-}$ mice (31), we delivered AAV2/9-hPPT1 intrathecally to target the spinal cord. We also combined this approach with brain-directed gene therapy (12, 24–27).

Consistent with previous studies, intracranial injection of an AAV2/9-hPPT1 vector resulted in a significantly increased life span, a preservation of motor function that we have shown previously to correlate with improved cerebellar pathology, and decreased pathology in the forebrain (12, 24–27). However, there was almost no improvement in spinal cord pathology following brain-directed gene therapy in *Ppt1*$^{-/-}$ mice. Conversely, intrathecal injection of AAV2/9-hPPT1 alone, despite having minimal impact upon pathology in the brain of these mice, significantly decreased pathology in the spinal cord, significantly increased life span, and improved motor function. The differential effects of these treatments are consistent with the reciprocal pattern of enzyme activity in these brain regions following IT vs. IC injections. Intrathecal injection resulted in ∼10% normal levels of PPT1 activity in the brain, and intracranial injections led to ∼5% normal levels of PPT1 activity in the spinal cord (Fig. 3*A*). Such enzyme levels might normally be sufficient to correct the disease phenotype in lysosomal storage diseases (41, 42). However, it may be that a higher

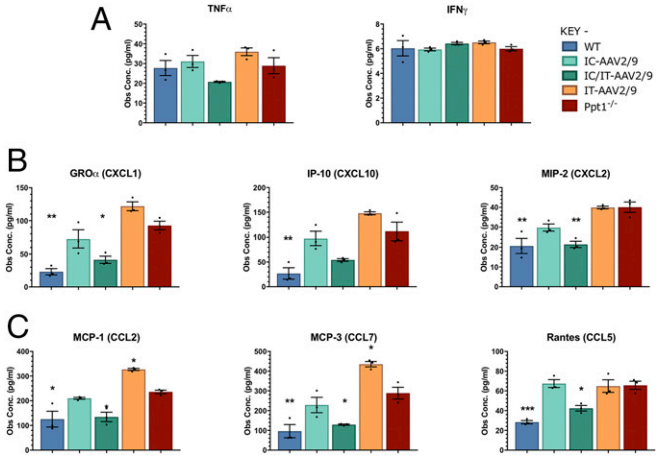

Fig. 8. Brain cytokine levels in treated animals at 7 mo. (*A*) The levels of various cytokines were measured in brain homogenates from treated and untreated WT and *Ppt1*$^{-/-}$ animals. There were no significant differences in the general proinflammatory cytokines TNF-α [with the exception of intrathecal (IT-AAV2/9) vs. combination intracranial/intrathecal (IC/IT-AAV2/9)] or IFN-γ between any of the groups. (*B*) Analysis of CXC-motif chemokines showed a significant increase in CXC-motif chemokines in *Ppt1*$^{-/-}$ and IT-AAV2/9 animals. IC/IT-AAV2/9 animals had a significant decrease in CXCL1 and CXCL2 at 7 mo. (*C*) CC-motif chemokines showed a significant increase in *Ppt1*$^{-/-}$ and IT-AAV2/9 mice. IC/IT-AAV2/9 animals had significantly decreased levels of CCL2, CCL7, and CCL5 at 7 mo. Overall, IC/IT-AAV2/9–treated mice showed chemokine levels similar to wild-type mice. Both CXC- and CC-motif chemokines are monocyte and leukocyte chemoattractive and activation molecules. Statistical comparisons were made with untreated *Ppt1*$^{-/-}$ mice. Values shown are mean ± SEM (*n* = 3 mice per group). Dots represent scatterplots of individual animals. **P* < 0.05, ***P* < 0.01, ****P* < 0.001, one-way ANOVA with post hoc Bonferroni correction.

level of PPT1 activity is required to achieve therapeutic benefit in CLN1 disease, and this may vary between brain regions.

No significant differences in cytokine or chemokine levels were observed in the brain between the IC-AAV2/9-hPPT1–treated mice and their untreated *Ppt1*$^{-/-}$ littermates, even though there was a decrease in histological markers of inflammation (CD68 and GFAP). Not surprisingly, there were no decreases in cytokine/chemokine levels in the brains of IT-AAV2/9-hPPT1–treated mice. In fact, the levels of MCP-1 and MCP-3 were significantly elevated in IT-AAV2/9–treated animals compared with untreated *Ppt1*$^{-/-}$ mice. Although the reason for this elevation is not clear, it could be an inflammatory response to the IT injection of virus that exacerbates the PPT1-associated neuroinflammation that is not corrected by IT-AAV2/9 alone. Taken together with the histological data, it appears that the effects of AAV gene therapy on cytokine/chemokine levels are localized to the areas of injection (Fig. 8). Indeed, in intracranially or intrathecally treated mice, there are clearly untreated regions of the CNS where the disease is still progressing. It seems likely that IC-treated animals have decreased cytokine/chemokine levels in certain areas of the brain. However, the untreated regions may still have high levels of cytokines/chemokines that overwhelm any regional reductions in a bulk sample of tissue. It is only when both the brain and spinal cord are treated that the elevated cytokines/chemokines return to nearly normal levels.

The differential clinical response of mice treated with either IC-AAV2/9 only or IT-AAV2/9 alone provides important insights into the progression of INCL. Targeting the spinal cord via IT-AAV2/9-hPPT1 corrected much of the pathology in the spinal cord but had little effect on the brain. Despite this, motor function was improved and the life span in these *Ppt1*$^{-/-}$ mice was significantly increased, even when histological correction was limited to the spinal cord. Such data suggest that this spinal pathology is clinically significant. However, it is unclear whether targeting the spinal cord also corrected other, yet unknown aspects of CLN1 disease such as any possible dorsal root ganglion (DRG) or peripheral nervous system pathology.

Our data suggest that although CLN1 disease significantly impacts the spinal cord, the brain remains the most severely and acutely affected region of the CNS in *Ppt1*$^{-/-}$ mice. Indeed, limiting therapy to the brain alone is clearly more effective than targeting the spinal cord alone. This study also clearly demonstrates that targeting the cerebral cortex, hippocampus, cerebellum, and spinal cord is not sufficient to correct the entire brain. As shown in this study, the thalamus is only partially corrected even when the brain and spinal cord are simultaneously targeted. It is likely that targeting the thalamus directly could further increase efficacy because it is a site of significant disease and it is the first region of the brain to be affected in CLN1 disease (14). Indeed, the thalamus consistently appears to be an important and early disease focus in many different LSDs, as is revealed by T2 imaging of these patients (43), and pronounced thalamic pathology has been shown in mouse models of all forms of NCL (reviewed in ref. 44) and all other LSDs we have examined (e.g., 45, 46). As such, it will be important to direct therapies to this brain region, and this may be key for improving therapeutic outcome further.

Combining intracranial and intrathecal injections of AAV2/9-hPPT1 led to dramatic and significant extension in life span and improvement in motor function compared with either therapy alone in *Ppt1*$^{-/-}$ mice. Indeed, IC/IT-AAV2/9-hPPT1–treated mice display the greatest biochemical, histological, and clinical improvements ever reported in CLN1 mice by a considerable margin. This is most likely due to the broader distribution of the AAV2/9-hPPT1 vector (and PPT1 enzyme levels) in the CNS. Taken together, these data suggest that it will be necessary to treat both the spinal cord and brain to achieve maximum efficacy. Interestingly, these data also show that targeting both the brain and spinal cord results in synergistic improvements. For example, if the modalities were simply additive, the predicted median life span would be ~16.7 mo rather than the ~19.3 mo observed. The similar improvement in motor function also suggests a synergistic effect, where the age at which the combination therapy mice begin to fall off the rotarod is greater than the sum of the increases observed with either intracranial or intrathecal treatment alone.

Although the combination therapy can dramatically and significantly increase life span and improve motor function, the IC/IT-AAV2/9-hPPT1–treated mice still have a reduced life span compared with their wild-type littermates, suggesting that these mice may be succumbing either to the residual pathology in regions of the CNS such as the thalamus or to disease outside of the central nervous system. There is a growing body of evidence for cardiac dysfunction (47–49) as well as systemic metabolic defects (50, 51) in CLN1 disease and other models of NCL. Targeting such additional sites of pathology and secondary disease mechanisms using other therapeutic modalities such as small-molecule drugs or recombinant PPT1 may further extend the life span and improve the quality of life for CLN1 disease patients.

This study clearly demonstrates the clinical significance of treating spinal cord pathology in CLN1 disease and has shown that AAV-mediated gene therapy can successfully prevent this when appropriately targeted. It remains to be seen how effective later administration of gene therapy would be, and it will be important to investigate this in future studies. However, our data reveal that a combination approach of IC/IT-AAV2/9-hPPT1 therapy has resulted in the greatest extension of life span and preservation of motor function in *Ppt1*$^{-/-}$ mice of any preclinical treatment so far (3, 28). Consistent with the current study, another group recently presented data in abstract form demonstrating that IT injection of a self-complementary AAV vector resulted in significant biochemical and clinical improvements in the *Ppt1*$^{-/-}$ mouse (52). Our data strongly suggest that the response could have been much greater if they had targeted both the brain and spinal cord. Recent clinical trials in children with other inherited neurological disorders such as CLN2, CLN6, giant axonal neuropathy, and spinal muscular atrophy using direct intracranial or intrathecal injections of AAV vectors (clinicaltrials.gov) have shown that these approaches are safe. As such, our findings will directly inform strategies for delivering therapies to children with this invariably fatal disease and other similar disorders in which spinal pathology may also occur.

Materials and Methods

Human Tissue. Paraffin wax-embedded tissue samples of human thoracic spinal cord were obtained from the archives of the Department of Pathology, Helsinki University and the Department of Pathology, Washington University School of Medicine. These specimens were collected at routine autopsies of CLN1 patients (n = 1, age of disease onset 1 y, age at death 6 y 10 mo) or neurologically normal controls (n = 1, age at death 10 y) with informed written consent and the approval of the Ethical Research Committee of the Institute of Psychiatry, Psychology & Neuroscience, King's College London (approval nos. 223/00 and 181/02).

Animals. Both congenic *Ppt1*$^{-/-}$ and wild-type mice were maintained on a C57BL/6J background at Washington University School of Medicine. The colonies were maintained separately through homozygous mating. All procedures were performed in accordance with NIH guidelines as well as a protocol approved by the Institutional Animal Care and Use Committee (IACUC) at Washington University School of Medicine. See *SI Materials and Methods* for further details.

Treatment Groups. For the analysis of spinal cord pathology, a sample size of n = 5 mice per group for wild-type C57BL/6 mice and *Ppt1*$^{-/-}$ were used at each time point of 1, 3, 5, and 7 mo as previously described (14). For the combination AAV2/9-hPPT1 therapy study, five treatment groups were generated: (*i*) untreated *Ppt1*$^{-/-}$ mice (n = 22), (*ii*) AAV2/9-hPPT1 intracranially injected *Ppt1*$^{-/-}$ mice (IC-AAV2/9-hPPT1, n = 25), (*iii*) AAV2/9-hPPT1 intrathecally injected *Ppt1*$^{-/-}$ mice (IT-AAV2/9-hPPT1, n = 25), (*iv*) combination AAV2/9-hPPT1 intracranially and intrathecally injected *Ppt1*$^{-/-}$ mice (IC/IT-AAV2/9-hPPT1, n = 25), and (*v*) wild-type C57BL/6 (n = 25) mice. We did not include a group of mice treated with a control AAV vector because we had already included this group in a prior study, and showed that intracranial injections of an AAV vector expressing GFP

had no effect on life span or any other parameter measured in *Ppt1*$^{-/-}$ mice (12). Longevity and rotarod performance were assessed in the treatment and control groups ($n = 10$ mice per group), and randomly selected mice were analyzed at predetermined time points (1, 3, 5, 7, and 9 mo) for biochemical and histological analyses ($n = 3$ mice per group). For all studies, experimental and control animals were randomly assigned identification numbers such that the person performing the analyses was blind to genotype and treatment, and all data collected are presented here.

Recombinant AAV Production. The rAAV2/9-hPPT1 vector genome used in this study is identical to that described and schematically represented previously (24), and was packaged at the University of North Carolina Vector Core. Viral titers were adjusted to 1×10^{12} vector genomes (vg)/mL for all injections. See *SI Materials and Methods* for further details.

Intracranial and Intrathecal Injections. On postnatal day 1 (PND1) or PND2, *Ppt1*$^{-/-}$ pups received intracranial or intrathecal injections with AAV2/9-hPPT1 (1×10^{12} vg/mL) into the anterior cortex, hippocampus, and cerebellum as previously described (12). For intrathecal injections, PND1 or PND2 *Ppt1*$^{-/-}$ pups were injected in the lumbar region as previously described (54, 55). For the combination treatment, both intracranial and intrathecal injections were performed on the same day in the same pup. See *SI Materials and Methods* for further details.

Life Span. Longevity was determined in the treatment and control groups ($n = 10$ mice per group) by death or euthanasia for humane reasons. A Kaplan–Meier life span curve was used to measure survival, and significant differences were determined using a log-rank analysis ($P < 0.05$).

Rotarod Testing. Motor function and coordination were assessed in the same treated *Ppt1*$^{-/-}$ and control mice ($n = 10$) used for longevity using a constant-speed (3 rpm) rotarod beginning at 5 mo of age and every 2 mo thereafter as previously described (12, 18). There was also a 3-d training/acclimation phase before the first test that allowed for a crude assessment of learning.

PPT1 Activity and Secondary Enzyme Elevations. Tissue was collected at predetermined time points (1, 3, 5, and 7 mo). Three mice per treatment group were euthanized via lethal injection (Fatal-Plus; Vortech Pharmaceuticals). PPT1 assays were performed on brain homogenates as previously described (56). Secondary elevations of another lysosomal enzyme, β-glucuronidase, were determined as previously described using a 4-methylumbelliferyl (MU)-β-D-glucuronide fluorometric assay and normalized to total protein (57). See *SI Materials and Methods* for further details.

Tissue Processing and Histological Staining. Brain processing and analysis were performed as previously described (11, 14, 25). Spinal cords were split into cervical, thoracic, and lumbosacral blocks. Forty-micrometer coronal sections were cut throughout each brain and spinal cord block and 5-μm-thick sections were cut from paraffin wax-embedded samples of human thoracic spinal cord. Sections were then stained for cresyl fast violet (Nissl) as before (11, 13) as a 1 in 6 series of brain sections or a 1 in 24 series of spinal cord sections to reveal cytoarchitecture. For immunohistochemistry, a 1 in 48 series of free-floating spinal cord sections from each mouse was stained using a standard immunoperoxidase protocol (11, 25) for markers of astrocytes (rabbit anti-GFAP; 1:8,000; Dako) and microglia (rat anti-mouse CD68; 1:2,000; AbD Serotec). Paraffin wax-embedded human spinal cord tissue sections were similarly immunostained as previously described (58) for monoclonal mouse anti-CD68 (clone PG-M1; 1:800; Dako).

Histochemical Stain. A histochemical stain for PPT1 activity was performed on sagittal forebrain sections and transverse sections of spinal cord, as previously described (35). See *SI Materials and Methods* for further details.

Visualization of Autofluorescent Storage Material. The accumulation of AFSM was visualized in unstained sections of tissue and quantified in different regions of the brain and spinal cord using a previously published method (24). See *SI Materials and Methods* for further details.

Stereological Analysis. Counts of neurons in the dorsal and ventral horns of each hemisection of the spinal cord were performed by a design-based optical fractionator method in a 1 in 48 series of Nissl-stained sections (59) using Stereo Investigator software (MBF Bioscience) (11). See *SI Materials and Methods* for further details.

Thresholding Image Analysis. To analyze the degree of glial activation in the gray matter of sections stained for GFAP and CD68, a semiautomated thresholding image analysis method was used with Image-Pro Premier software (Media Cybernetics) (11). See *SI Materials and Methods* for further details.

Cytokine Profile Analysis. Cytokine profiling was performed using an Affymetrix multiplex assay through the Center for Human Immunology and Immunotherapy Programs (CHiiPS) Immunomonitoring Lab (IML) at Washington University School of Medicine. Nine analytes (GRO-α, IFN-γ, IL-10, IP-10, MCP-1, MCP-3, MIP-2, RANTES, and TNF-α) were measured in brain homogenates of treated animals. See *SI Materials and Methods* for further details.

Statistical Analysis. All statistical analyses were performed using Prism software (GraphPad Software). A two-tailed, unpaired, parametric *t* test was used where two groups were compared, and a one-way ANOVA with a Bonferroni post hoc analysis was used when comparing three or more groups at each time point. Results were considered statistically significant when $P < 0.05$. Unless otherwise stated, statistical comparisons are between the treatment groups and untreated *Ppt1*$^{-/-}$ mice. The mean coefficient of error for all stereological measures was below 0.10 (60), and all measurements were performed blind to genotype.

ACKNOWLEDGMENTS. The authors acknowledge Sarmi Sri, Jasmyn Dmytrus, and Sioned Williams for generating preliminary data for spinal cord pathology. We also thank Drs. John Østergaard, Patricia Dickson, Elizabeth Bradbury, and Alison Barnwell for their advice and comments on the manuscript. This work was supported by NIH NINDS 043205 (to M.S.S. and J.D.C.) and a King's College London Graduate School International Studentship Award (to H.R.N.).

1. Jalanko A, Braulke T (2009) Neuronal ceroid lipofuscinoses. *Biochim Biophys Acta* 1793:697–709.
2. Warrier V, Vieira M, Mole SE (2013) Genetic basis and phenotypic correlations of the neuronal ceroid lipofusinoses. *Biochim Biophys Acta* 1832:1827–1830.
3. Geraets RD, et al. (2016) Moving towards effective therapeutic strategies for neuronal ceroid lipofuscinosis. *Orphanet J Rare Dis* 11:40.
4. Santavuori P, Haltia M, Rapola J (1974) Infantile type of so-called neuronal ceroid-lipofuscinosis. *Dev Med Child Neurol* 16:644–653.
5. Vesa J, et al. (1995) Mutations in the palmitoyl protein thioesterase gene causing infantile neuronal ceroid lipofuscinosis. *Nature* 376:584–587.
6. Camp LA, Hofmann SL (1993) Purification and properties of a palmitoyl-protein thioesterase that cleaves palmitate from H-Ras. *J Biol Chem* 268:22566–22574.
7. Lu JY, Verkruyse LA, Hofmann SL (1996) Lipid thioesters derived from acylated proteins accumulate in infantile neuronal ceroid lipofuscinosis: Correction of the defect in lymphoblasts by recombinant palmitoyl-protein thioesterase. *Proc Natl Acad Sci USA* 93:10046–10050.
8. Santavuori P, Haltia M, Rapola J, Raitta C (1973) Infantile type of so-called neuronal ceroid-lipofuscinosis. 1. A clinical study of 15 patients. *J Neurol Sci* 18:257–267.
9. Mole SE, Williams RE, Goebel HH (2005) Correlations between genotype, ultrastructural morphology and clinical phenotype in the neuronal ceroid lipofuscinoses. *Neurogenetics* 6:107–126.
10. Gupta P, et al. (2001) Disruption of PPT1 or PPT2 causes neuronal ceroid lipofuscinosis in knockout mice. *Proc Natl Acad Sci USA* 98:13566–13571.
11. Bible E, Gupta P, Hofmann SL, Cooper JD (2004) Regional and cellular neuropathology in the palmitoyl protein thioesterase-1 null mutant mouse model of infantile neuronal ceroid lipofuscinosis. *Neurobiol Dis* 16:346–359.
12. Griffey MA, et al. (2006) CNS-directed AAV2-mediated gene therapy ameliorates functional deficits in a murine model of infantile neuronal ceroid lipofuscinosis. *Mol Ther* 13:538–547.
13. Kühl TG, Dihanich S, Wong AM, Cooper JD (2013) Regional brain atrophy in mouse models of neuronal ceroid lipofuscinosis: A new rostrocaudal perspective. *J Child Neurol* 28:1117–1122.
14. Kielar C, et al. (2007) Successive neuron loss in the thalamus and cortex in a mouse model of infantile neuronal ceroid lipofuscinosis. *Neurobiol Dis* 25:150–162.
15. Macauley SL, et al. (2009) Cerebellar pathology and motor deficits in the palmitoyl protein thioesterase 1-deficient mouse. *Exp Neurol* 217:124–135.
16. Kielar C, et al. (2009) Molecular correlates of axonal and synaptic pathology in mouse models of Batten disease. *Hum Mol Genet* 18:4066–4080.
17. Santavuori P, et al. (1993) Infantile neuronal ceroid-lipofuscinosis (INCL): Diagnostic criteria. *J Inherit Metab Dis* 16:227–229.
18. Dearborn JT, et al. (2015) Comprehensive functional characterization of murine infantile Batten disease including Parkinson-like behavior and dopaminergic markers. *Sci Rep* 5:12752.
19. Wei H, et al. (2011) Disruption of adaptive energy metabolism and elevated ribosomal p-S6K1 levels contribute to INCL pathogenesis: Partial rescue by resveratrol. *Hum Mol Genet* 20:1111–1121.

20. Sarkar C, et al. (2013) Neuroprotection and lifespan extension in Ppt1(–/–) mice by NtBuHA: Therapeutic implications for INCL. *Nat Neurosci* 16:1608–1617.
21. Lu JY, Hu J, Hofmann SL (2010) Human recombinant palmitoyl-protein thioesterase-1 (PPT1) for preclinical evaluation of enzyme replacement therapy for infantile neuronal ceroid lipofuscinosis. *Mol Genet Metab* 99:374–378.
22. Hu J, et al. (2012) Intravenous high-dose enzyme replacement therapy with recombinant palmitoyl-protein thioesterase reduces visceral lysosomal storage and modestly prolongs survival in a preclinical mouse model of infantile neuronal ceroid lipofuscinosis. *Mol Genet Metab* 107:213–221.
23. Tamaki SJ, et al. (2009) Neuroprotection of host cells by human central nervous system stem cells in a mouse model of infantile neuronal ceroid lipofuscinosis. *Cell Stem Cell* 5:310–319.
24. Griffey M, et al. (2004) Adeno-associated virus 2-mediated gene therapy decreases autofluorescent storage material and increases brain mass in a murine model of infantile neuronal ceroid lipofuscinosis. *Neurobiol Dis* 16:360–369.
25. Macauley SL, et al. (2012) Synergistic effects of central nervous system-directed gene therapy and bone marrow transplantation in the murine model of infantile neuronal ceroid lipofuscinosis. *Ann Neurol* 71:797–804.
26. Roberts MS, et al. (2012) Combination small molecule PPT1 mimetic and CNS-directed gene therapy as a treatment for infantile neuronal ceroid lipofuscinosis. *J Inherit Metab Dis* 35:847–857.
27. Macauley SL, et al. (2014) An anti-neuroinflammatory that targets dysregulated glia enhances the efficacy of CNS-directed gene therapy in murine infantile neuronal ceroid lipofuscinosis. *J Neurosci* 34:13077–13082.
28. Hawkins-Salsbury JA, Cooper JD, Sands MS (2013) Pathogenesis and therapies for infantile neuronal ceroid lipofuscinosis (infantile CLN1 disease). *Biochim Biophys Acta* 1832:1906–1909.
29. Passini MA, et al. (2006) Intracranial delivery of CLN2 reduces brain pathology in a mouse model of classical late infantile neuronal ceroid lipofuscinosis. *J Neurosci* 26:1334–1342.
30. Katz ML, et al. (2015) AAV gene transfer delays disease onset in a TPP1-deficient canine model of the late infantile form of Batten disease. *Sci Transl Med* 7:313ra180.
31. Lu JY, et al. (2015) Intrathecal enzyme replacement therapy improves motor function and survival in a preclinical mouse model of infantile neuronal ceroid lipofuscinosis. *Mol Genet Metab* 116:98–105.
32. Dayton RD, Wang DB, Klein RL (2012) The advent of AAV9 expands applications for brain and spinal cord gene delivery. *Expert Opin Biol Ther* 12:757–766.
33. Swain GP, et al. (2014) Adeno-associated virus serotypes 9 and rh10 mediate strong neuronal transduction of the dog brain. *Gene Ther* 21:28–36.
34. Haltia M, Rapola J, Santavuori P (1973) Infantile type of so-called neuronal ceroid-lipofuscinosis. Histological and electron microscopic studies. *Acta Neuropathol* 26:157–170.
35. Dearborn JT, et al. (2016) Histochemical localization of palmitoyl protein thioesterase-1 activity. *Mol Genet Metab* 117:210–216.
36. Macauley SL, Pekny M, Sands MS (2011) The role of attenuated astrocyte activation in infantile neuronal ceroid lipofuscinosis. *J Neurosci* 31:15575–15585.
37. Qiao X, Lu JY, Hofmann SL (2007) Gene expression profiling in a mouse model of infantile neuronal ceroid lipofuscinosis reveals upregulation of immediate early genes and mediators of the inflammatory response. *BMC Neurosci* 8:95.
38. Anderson GW, Goebel HH, Simonati A (2013) Human pathology in NCL. *Biochim Biophys Acta* 1832:1807–1826.
39. Katz ML, et al. (2014) Enzyme replacement therapy attenuates disease progression in a canine model of late-infantile neuronal ceroid lipofuscinosis (CLN2 disease). *J Neurosci Res* 92:1591–1598.
40. Foust KD, et al. (2009) Intravascular AAV9 preferentially targets neonatal neurons and adult astrocytes. *Nat Biotechnol* 27:59–65.
41. Neufeld EF, Fratantoni JC (1970) Inborn errors of mucopolysaccharide metabolism. *Science* 169:141–146.
42. Donsante A, Levy B, Vogler C, Sands MS (2007) Clinical response to persistent, low-level beta-glucuronidase expression in the murine model of mucopolysaccharidosis type VII. *J Inherit Metab Dis* 30:227–238.
43. Autti T, Joensuu R, Aberg L (2007) Decreased T2 signal in the thalami may be a sign of lysosomal storage disease. *Neuroradiology* 49:571–578.
44. Cooper JD, Tarczyluk MA, Nelvagal HR (2015) Towards a new understanding of NCL pathogenesis. *Biochim Biophys Acta* 1852:2256–2261.
45. Pressey SN, Smith DA, Wong AM, Platt FM, Cooper JD (2012) Early glial activation, synaptic changes and axonal pathology in the thalamocortical system of Niemann-Pick type C1 mice. *Neurobiol Dis* 45:1086–1100.
46. Farfel-Becker T, et al. (2011) Spatial and temporal correlation between neuron loss and neuroinflammation in a mouse model of neuronopathic Gaucher disease. *Hum Mol Genet* 20:1375–1386.
47. Galvin N, et al. (2008) A murine model of infantile neuronal ceroid lipofuscinosis-ultrastructural evaluation of storage in the central nervous system and viscera. *Pediatr Dev Pathol* 11:185–192.
48. Ostergaard JR, Rasmussen TB, Mølgaard H (2011) Cardiac involvement in juvenile neuronal ceroid lipofuscinosis (Batten disease). *Neurology* 76:1245–1251.
49. Fukumura S, et al. (2012) Progressive conduction defects and cardiac death in late infantile neuronal ceroid lipofuscinosis. *Dev Med Child Neurol* 54:663–666.
50. Woloszynek JC, Coleman T, Semenkovich CF, Sands MS (2007) Lysosomal dysfunction results in altered energy balance. *J Biol Chem* 282:35765–35771.
51. Khaibullina A, et al. (2012) In a model of Batten disease, palmitoyl protein thioesterase-1 deficiency is associated with brown adipose tissue and thermoregulation abnormalities. *PLoS One* 7:e48733.
52. Rozenberg AJ, Gray SJ (2017) Early intrathecal gene therapy extends lifespan and improves quality of life in a mouse model for infantile neuronal ceroid lipofuscinosis. *Mol Genet Metab* 120:S117.
53. Cooper JD, Russell C, Mitchison HM (2006) Progress towards understanding disease mechanisms in small vertebrate models of neuronal ceroid lipofuscinosis. *Biochim Biophys Acta* 1762:873–889.
54. Elliger SS, Elliger CA, Aguilar CP, Raju NR, Watson GL (1999) Elimination of lysosomal storage in brains of MPS VII mice treated by intrathecal administration of an adeno-associated virus vector. *Gene Ther* 6:1175–1178.
55. Hawkins-Salsbury JA, et al. (2015) Mechanism-based combination treatment dramatically increases therapeutic efficacy in murine globoid cell leukodystrophy. *J Neurosci* 35:6495–6505.
56. van Diggelen OP, et al. (1999) A rapid fluorogenic palmitoyl-protein thioesterase assay: Pre- and postnatal diagnosis of INCL. *Mol Genet Metab* 66:240–244.
57. Sands MS, et al. (1994) Enzyme replacement therapy for murine mucopolysaccharidosis type VII. *J Clin Invest* 93:2324–2331.
58. Tyynelä J, Cooper JD, Khan MN, Shemilts SJ, Haltia M (2004) Hippocampal pathology in the human neuronal ceroid-lipofuscinoses: Distinct patterns of storage deposition, neurodegeneration and glial activation. *Brain Pathol* 14:349–357.
59. West MJ, Slomianka L, Gundersen HJ (1991) Unbiased stereological estimation of the total number of neurons in the subdivisions of the rat hippocampus using the optical fractionator. *Anat Rec* 231:482–497.
60. Gundersen HJ, Jensen EB (1987) The efficiency of systematic sampling in stereology and its prediction. *J Microsc* 147:229–263.